Journal of Metals, Materials and Minerals, 36(4), e2690, 2026

FDM-based fabrication of flexible CNT/TPU strain sensors with optimized infill patterns and ultrasonication CNT coating for wearable health monitoring

Siriporn WU[1], Nutthapong POOMPIEW[1], Pranut POTIYARAJ[1,3], Chuanchom AUMNATE[3,4] and Patrapee KUNGSADALPIPOB[1,2,*]

[1] *Department of Materials Science, Faculty of Science, Chulalongkorn University, Bangkok 10330 Thailand*
[2] *Center of Excellence in Upcycled Materials from Industrial and Agricultural Wastes, Faculty of Science Chulalongkorn University, Bangkok 10330 Thailand*
[3] *Center of Excellence in Responsive Wearable Materials, Faculty of Science, Chulalongkorn University, Bangkok 10330 Thailand*
[4] *The Petroleum and Petrochemical College, Chulalongkorn University, Bangkok 10330 Thailand*

***Corresponding author e-mail**: patrapee.k@chula.ac.th

Received date:
31 March 2026
Revised date:
14 May 2026
Accepted date:
5 June 2026

Keywords:
Strain sensor;
3D printing;
Carbon nanotubes (CNTs);
Wearable electronics;
Motion detection

Abstract

Wearable motion sensors have become essential tools for monitoring human movement across a broad range of health applications. In this study, flexible strain sensors were developed using 3D-printed thermoplastic polyurethane (TPU) substrates combined with carbon nanotubes (CNTs). Three internal architectures: triangle (TR), grid (GD), and honeycomb (HN) with infill densities ranging from 10% to 20% were fabricated using fused deposition modeling (FDM) to investigate the influence of structural design on mechanical and sensing performance. Conductivity was achieved by an ultrasonication cavitation-assisted CNT deposition followed by thermal treatment, enabling CNT attachment on TPU surfaces and partial penetration into interlayer gaps. SEM analysis confirmed the formation of a rough CNT-coated surface providing conductive pathways for strain sensing. Mechanical testing showed that infill pattern strongly influenced deformation behavior, with the honeycomb structure demonstrating greater structural compliance and elongation than other patterns. Among all configurations, the C-HN10 sample (honeycomb infill with 10% density) demonstrated the best sensing performance, achieving a gauge factor of 9.283 in the low-strain region while exhibiting stable cyclic responses. The optimized sensor maintained repeatable electrical signals under bending deformation and when integrated into body-motion monitoring wearable bands. These results demonstrate that pattern control of FDM-printed structures provides an effective strategy for tuning the mechanical flexibility and sensitivity of CNT-coated TPU strain sensors, offering a scalable method for developing wearable motion-tracking devices.

1. Introduction

Wearable and soft electronic systems increasingly rely on deformable sensors that can convert mechanical motion into stable electrical signals for applications such as human-machine interfaces, rehabilitation monitoring, sports biomechanics, soft robotics, and continuous health tracking. Among the available modalities, strain sensors are particularly important because many real-world signals of interest such as joint bending, muscle bulging, respiration, posture, are fundamentally elongational deformation rather than other axial loading [1]. A practical wearable strain sensor must simultaneously meet requirements that are often competing high stretchability, good linearity, fast response-recovery, mechanical stability under thousands of cycles, and manufacturability in customizable form factors [2,3]. Studies of stretchable and wearable strain sensors consistently emphasize that device performance is not determined solely by the conductive filler chemistry, but also by the mechanics-microstructure coupling that governs how conductive pathways evolve under strain [4,5]. A widely adopted approach for flexible strain sensing is the piezoresistive polymer composite, where conductive networks such as carbon nanotubes (CNTs), graphene, metal nanowires are embedded within an elastomeric matrix.The sensor output is typically measured as a resistance change with applied strain, arising from deformation-induced rearrangement of conductive pathways, variation in tunneling distances between adjacent fillers, and microcrack formation or closure depending on material structure [6,7]. In particular, carbon nanotubes (CNTs) stand out due to their high aspect ratio and ability to form percolated networks at relatively low loading, enabling stretchable conductors that remain functional even when the polymer matrix undergoes significant deformation. The sensitivity and working range of CNT-based composites have been reported to be strongly influenced by filler dispersion, filler-polymer interfacial interaction, and mesoscale structural features that control how strain is localized within the conductive network [8–10].

Among elastomeric matrices, thermoplastic polyurethane (TPU) is especially compelling for wearable strain sensors because it combines elasticity, abrasion resistance, and processability as a thermoplastic filament. When combined with CNT fillers, TPU-based nanocomposites can achieve large deformability while maintaining a conductive network that responds to strain. Several studies have demonstrated that CNT/TPU systems can deliver high sensitivity and broad sensing range when dispersion and interfacial interaction are optimized [11–13]. A key bottleneck is translating CNT/TPU strain sensors into real devices that are practical to manufacture. Conventional fabrication routes such as casting, screen printing or molding can produce functional sensors, but they often limit geometric customization, are labor-intensive for iterative design, and can be sensitive to operator variability. In contrast, additive manufacturing (AM) offers a path toward digital, scalable fabrication of wearable sensors with tunable geometries. Fused deposition modeling (FDM) is widely available, cost-effective, and compatible with TPU-based filaments. FDM enables not only rapid prototyping of sensor shape but also fine control of internal mesoscale architecture through toolpath strategy and infill parameters. This geometric programmability is increasingly recognized as a design lever for functional properties of soft electronics, where internal porosity, strut orientation, and cellular topology can be engineered to tailor mechanical properties and sensitivity [14,15]. Importantly, FDM printing introduces microstructural features such as layer-by-layer interfaces, raster orientation, void distribution, and mesostructural infill that can substantially affect both mechanical behavior and electromechanical performance. Previous studies have shown that CNT/TPU feedstocks for FDM are typically produced by dispersing CNTs throughout the TPU matrix, most commonly via 1) melt compounding (where CNT powder is blended with TPU under high shear and high temperature input in an internal mixer or single/ twin screw extruder) [16-18], 2) solvent-assisted dispersion (where CNT are dispersed using a solvent and ultrasonic agitation, followed by drying, and then the resulting nanocomposite is extruded into a diameter-controlled filament for printing [19–20]. For example, Christ *et al.* compounded CNT/TPU, extruded the composite into filaments, and the printed strain sensing specimens using FDM [21], while other CNT/TPU for FDM printing studies further improved CNT-TPU interfacial compatibility and dispersion using pyrene-based noncovalent modifiers prior to filament extrusion, which helped generate a more uniform conductive network and improved electromechanical performance [22]. Recent studies have also reported hybrid processing routes such as solution casting combined with twin-screw extrusion to prepare printable CNT/TPU filament illustrating that both dispersion strategy and extrusion history are central to achieving printable rheology and resulting, stable strain response in CNT/TPU sensors [23].

Despite these advances, existing CNT/TPU 3D printing studies still leave several practical gaps when designing reliable wearable strain sensors. In many reports, CNT incorporation route is only briefly described, making it difficult to reproduce dispersion quality, filament rheology, and the resulting conductive network stability. Moreover, most demonstrations emphasize overall sensitivity but provide limited explanation of how printing-induced architecture shapes current-flow pathways and signal drift under repeated deformation. Critically for wearable motion sensing, systematic comparisons of 3D-printing design parameters, especially infill structure and the resulting deformation behavior, remain scarce, and many characterizations are performed under loading conditions that do not fully represent cyclic stretching in real use. To address these limitations, this work focuses on building more uniform and repeatable conductive pathways in FDM-printed CNT/TPU by optimizing printing conditions and integrating an ultrasonic cavitation-enabled treatment with a thermal-assisted approach uniform conductive pathways in CNT/TPU prints, and to qualitatively evaluate how these process parameters influence the structural features and electromechanical strain sensing performance under cyclic deformation, with the goal of establishing practical approach for designing repeatable, high-performance CNT-TPU wearable strain sensors.

2. Experimental

2.1 Materials

A commercial TPU filament (95A hardness, 1.75 mm diameter) was obtained from Neotech Co., Ltd. (Thailand) and used as a reference material. Carbon nanotubes (CNTs) were purchased from Nano Generation Co., Ltd (Thailand) and employed as the conductive fillers.

2.2 3D printing of TPU and CNT-coated TPU substrates

TPU substrates were fabricated by fused deposition modeling (FDM) using a WANHAO Duplicator 9 printer. The samples were designed and printed using MatterControl 2.0 (MatterHackers, Inc., USA), with the printing parameters summarized in Table 1. To investigate the influence of internal architecture on mechanical and electrical performance, three infill patterns: honeycomb (HN), triangle (TR), and grid (GD) were selected (Figure 1(a)) and printed at infill densities of 10%, 15%, and 20%.

2.3 Post-print CNT incorporation

To introduce conductivity, the printed TPU substrates were treated with carbon nanotubes (CNTs) by depositing CNTs onto the substrate surface, as shown in Figure 1(b). CNTs were first dispersed in deionized (DI) water using an ultrasonic liquid processor (Sonics Vibra-Cell VCX 750, Sonics & Materials Inc., USA). An ultrasonic probe was immersed in a 1% w/v CNT dispersion, and cavitation-assisted dispersion was carried out for 60 min. The selected CNT concentration was based on our previous work [24], where the same ultrasonication-assisted coating approach demonstrated stable conductive network formation, uniform coating distribution, and reliable electromechanical performance on 3D-printed TPU substrates. After coating, the CNT-treated TPU samples were dried in an oven at 30°C for 6 h to remove residual moisture. Next, the samples were heated in a vacuum oven at 120°C for 24 h to facilitate CNT penetration into the interlayer gaps formed during the 3D-printing process [25]. Finally, the samples were cooled to ambient temperature for 24 h to complete fabrication. The fabricated samples were designated based on the infill pattern, infill density, and CNT coating condition, as summarized in Table 2.

2.4 Characterization of 3D-printed CNT-coated TPU substrates

2.4.1 Morphology characterization and elemental analysis

The surface morphology of the 3D-printed TPU samples before and after CNT incorporation was investigated using scanning electron microscopy (SEM, JEOL JEM-7000). SEM imaging was performed at an accelerating voltage of 15 kV with a magnification of 30x to 250x.

The instrument was equipped with an energy dispersive X-ray spectrometer (EDS), which was used to characterize the elemental composition of the samples. EDS analysis was conducted at 15 kV with a magnification of 30x. These measurements were performed to confirm the presence of CNTs on the sample surface.

2.4.2 Mechanical testing

Quasi-static tensile testing was performed in accordance with ASTM D412 using a universal testing machine (Tinius Olsen, Model 5ST). Tests were conducted with a 5 kN load cell, a crosshead speed of 10 mm·s^{-1}, and a gauge length of 4 mm. Each condition was tested five times, and reported values are presented as the average of five measurements. The mechanical properties were recorded automatically by the instrument and used to determine the tensile strength and tensile modulus.

2.4.3 Electromechanical testing

A potentiostat (PalmSens BV, PalmSens4) was used to investigate the electromechanical properties of the samples by recording the current response during tensile deformation. Measurements were performed at a constant applied voltage of 1 V, and the electrical signal was reported as the normalized current change, $\Delta I/I_0$ (%), where I_0 is the baseline current at the unstrained state. Because the device functions as a strain sensors, performance was quantified using the gauge factor (GF), defined as the ratio of relative signal change to the applied strain:

$$GF = \frac{\Delta(I/I_0)}{\Delta\varepsilon} \qquad (1)$$

Where $\Delta(I/I_0)$ is the change in normalized current and $\Delta\varepsilon$ is the applied strain.

In addition, the potentiostat was used to record the real-time I/I_0 (%) response of the sensor under cyclic tensile loading and unloading. The effect of strain amplitude was evaluated at 10%, 15%, 20%, 25%, and 30% elongation at a crosshead speed of 10 mm·min^{-1}. The effect of deformation rate was investigated at 30% elongation under crosshead speeds of 10 mm·min^{-1}, 15 mm·min^{-1}, 20 mm·min^{-1}, 25 mm·min^{-1}, and 30 mm·min^{-1}. The fabricated strain sensors were sewn onto a wearable band and positioned at four joint locations for finger bending, elbow flexion, knee bending, and achilles flexing to evaluate real-time performance during motion, where the sensors underwent repeated straining and releasing as the joints moved. The human-subject test protocol received ethical approval from the Research Involving Human Research Participants, Group I, Chulalongkorn University, Thailand (COA No. 119/68).

Table 1. Controlled printing parameters for substrate preparation.

Parameter	Controlled setup
Nozzle temperature	210°C
Bed temperature	60°C
Printing speed	15 mm·s^{-1}
Nozzle diameter	0.4 mm
Layer thickness	0.4 mm
Number of perimeters	1
Starting angle	0°

Table 2. Sample nomenclature and composition of pure and CNT-coated TPU substrates based on infill pattern and density

Sample	Infill pattern	infill density (%)	Conductive Coating (%w/v)
P-TR10	triangle	10	-
C-TR10			1% CNT
P-TR15		15	-
C-TR15			1% CNT
P-TR20		20	-
C-TR20			1% CNT
P-GD10	grid	10	-
C-GD10			1% CNT
P-GD15		15	-
C-GD15			1% CNT
P-GD20		20	-
C-GD20			1% CNT
P-HN10	honeycomb	10	-
C-HN10			1% CNT
P-HN15		15	-
C-HN15			1% CNT
P-HN20		20	-
C-HN20			1% CNT

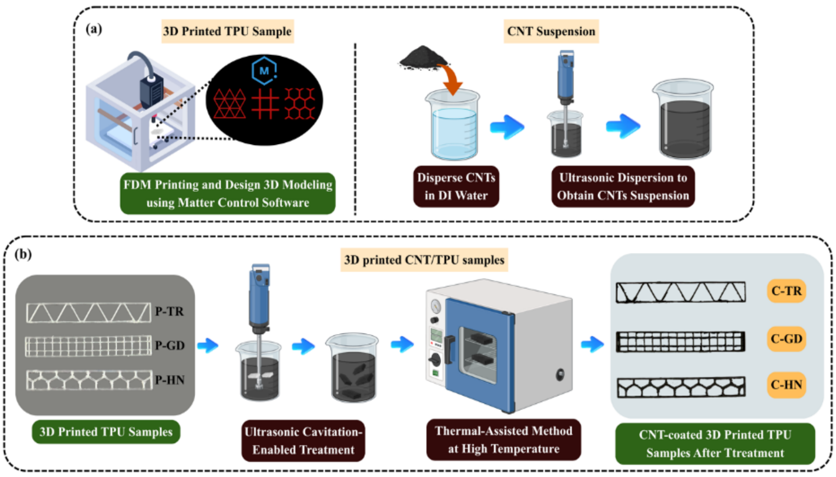

Figure 1. Strain sensor preparation: (a) 3D-printing of TPU substrate and preparation of CNT dispersion, (b) incorporation of CNTs via ultrasonication and thermal-assisted treatment.

3. Results and discussion

3.1 Morphological and elemental analysis

The surface morphology and elemental composition of the 3D-printed TPU substrates before and after CNT incorporation were investigated using scanning electron microscope (SEM) and energy dispersive X-ray spectroscopy (EDS), as shown in Figure 2 and Table 3, respectively. The SEM images compare the pristine TPU structures (P-TR10, P-GD10, and P-HN10) with the corresponding CNT-treated samples (C-TR10, C-GD10, and C-HN10) to evaluate the effect of CNT deposition on the printed substrates.

EDS analysis confirmed significant changes in elemental composition after CNT treatment. For the pristine TPU samples, the carbon content was relatively consistent across all infill patterns, ranging from 40.92% to 41.49%, while the oxygen content remained comparatively higher due to the oxygen containing functional groups present in the polyurethane structure. After CNT incorporation, the carbon content increased significantly approximately 54.04% to 57.47%, while the oxygen content correspondingly decreased. This compositional change confirms successful CNT deposition on the TPU substrates, since CNTs are predominantly composed of carbon. Among the investigated samples, the honeycomb structure exhibited the highest carbon content, suggesting improved CNT retention or accumulation during the ultrasonication-assisted treatment process.

The pristine TPU samples (Figure 2(a,c,e)) exhibit relatively smooth surfaces with clearly defined printing paths and junction nodes generated during the FDM process. Continuous cylindrical printed lines and well-formed intersections corresponding to the designed infill structures can be observed, indicating that the selected printing conditions produced well-defined internal architectures without major structural defects.

After CNT incorporation, the treated samples (Figure 2(b,d,f)) show a noticeably rougher surface morphology compared with the pristine TPU structures. A thin particulate and network-like layer can be observed coating the printed line. At higher magnification (250x), aggregated CNT clusters can be observed on the TPU surfaces, forming conductive coating regions along the printed lines, as indicated in Figure 2. This observation is consistent with the increased carbon content obtained from EDS analysis and confirms successful attachment of CNTs during the ultrasonic cavitation and thermal-assisted treatment process.

The CNT coating appears relatively uniform across the different infill patterns, although slight variations in surface roughness can be observed near printed junctions where multiple printed strands intersect. These regions provide additional surface area and micro-gaps formed during the layer-by-layer FDM process, which may facilitate CNT accumulation and penetration during ultrasonication. In addition, the thermal-assisted treatment likely increased TPU chain mobility, allowing partial embedding of CNTs into the polymer surface and interlayer gaps. These microstructural features are beneficial for electromechanical sensing performance because the deposited CNT network forms conductive pathways along the printed line. During tensile deformation, the relative spacing between neighboring CNT cluster changes, altering the electrical current flow through the network. Therefore, the combined SEM and EDS results confirm that the ultrasonication-assisted deposition method successfully produced conductive CNT-coated TPU substrate suitable for strain-sensing applications.

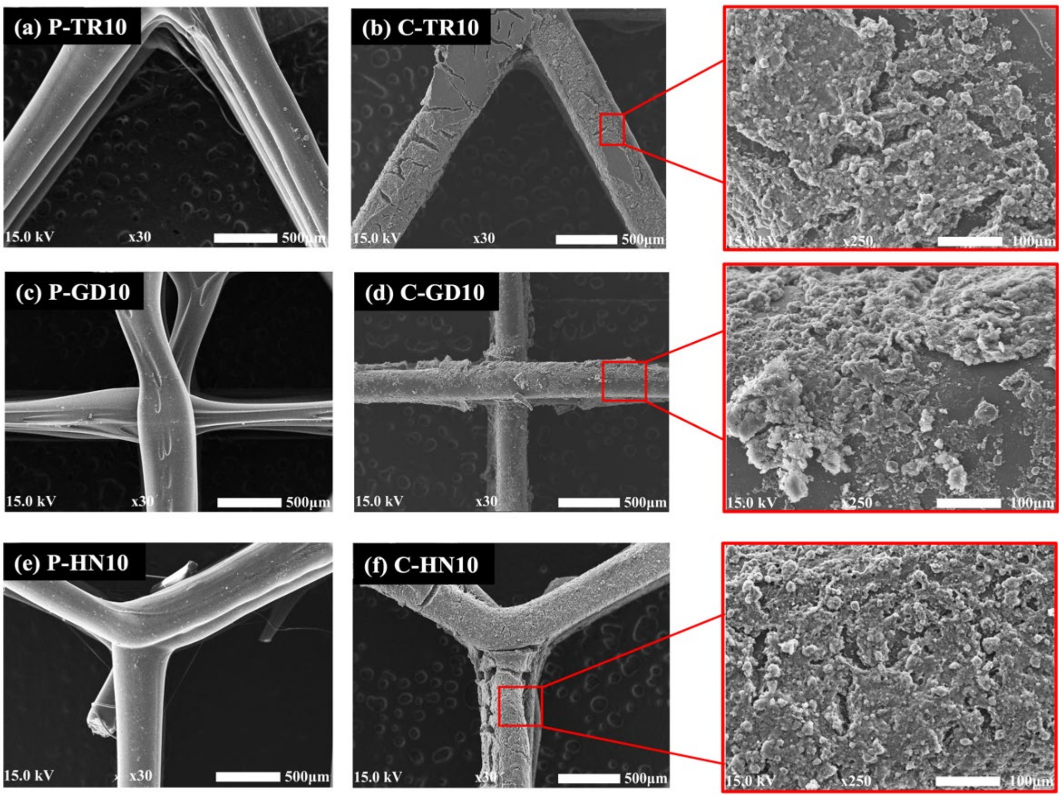

Figure 2. SEM micrographs of (a-b) triangle, (c-d) grid, and (e-f) honeycomb infilled substates, comparing samples before and after CNT incorporation.

Table 3. Elemental composition of samples before and after CNT incorporation determined by EDS analysis.

Sample	Weight (%)	
	C	O
P-TR10	41.35 ± 3.30	58.65 ± 8.34
C-TR10	56.31 ± 1.78	43.69 ± 4.11
P-GD10	40.92 ± 3.47	59.08 ± 8.75
C-GD10	54.05 ± 1.58	45.95 ± 3.70
P-HN10	41.49 ± 1.33	58.51 ± 3.36
C-HN10	57.47 ± 1.92	42.26 ± 4.38

3.2 Tensile properties

The tensile stress-strain curves of the 3D-printed TPU substrate with triangle (C-TR), grid (C-GD), and honeycomb (C-HN) infill pattern at different densities (10% to 20%) are shown in Figure 3(a-c), and corresponding data are reported in Table 4. All samples exhibited a typical elastomeric response characterized by an initial nonlinear region at low strain followed by gradual strain hardening until failure. The printed structures demonstrated excellent stretchability, with elongation between 514% to 740%, indicating that the TPU matrix retained its high elasticity after FDM printing, and the CNT coating. The CNT coating process in this work was primarily intended to introduce conductive pathways on the TPU surface rather than reinforce the bulk TPU matrix. Therefore, the overall tensile behavior was mainly governed by the internal infill pattern and deformation characteristics of the TPU structures. Previous work by Li *et al*. demonstrated that ultrasonication cavitation-assisted CNT incorporation mainly modified strength because the CNTs are deposited on the surface rather than incorporated into the bulk polymer matrix [25].

For the triangle pattern (Figure 3(a)), the maximum tensile stresses were approximately 12.87 MPa (C-TR10), 11.51 MPa (C-TR15), and 12.54 MPa (C-TR20). The elongation at break ranged from 430-550%, with C-TR10 exhibiting the highest ultimate strength among the C-TR samples. The triangular geometry distributes stress through angled printed line connections, which can promote progressive deformation but may also introduce localized stress concentration at line junctions. Although increasing infill density generally increases

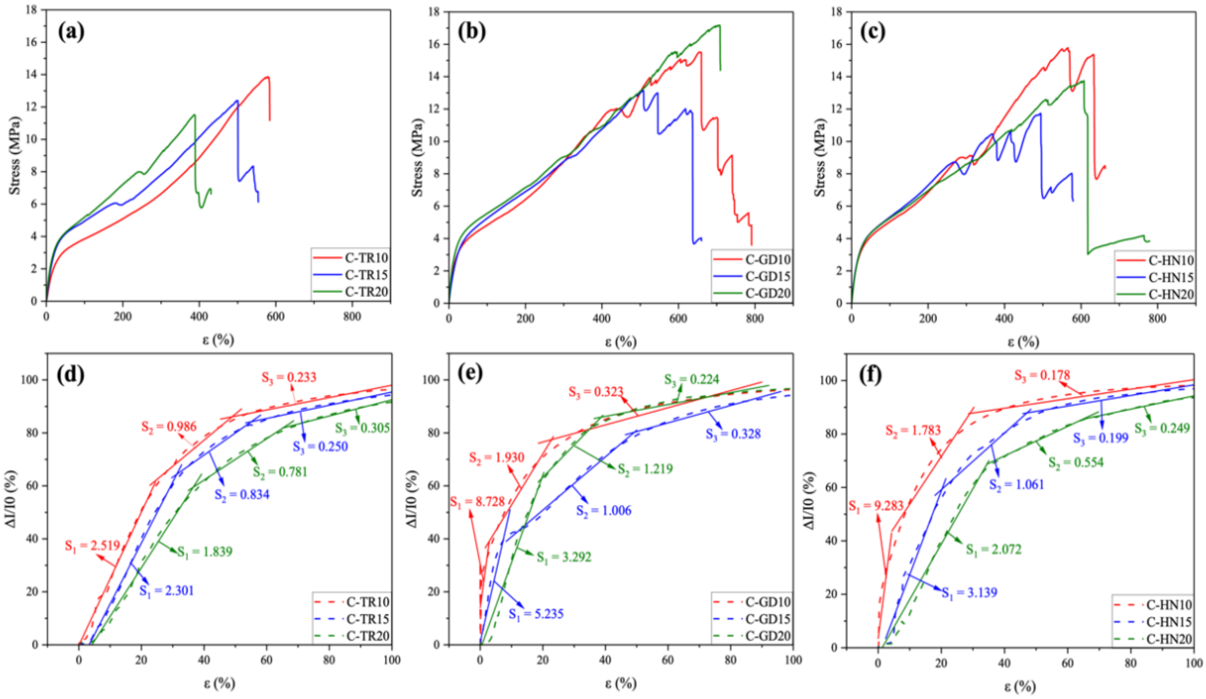

Figure 3. Tensile properties of (a) triangle, (b) grid, and (c) honeycomb infilled samples, and electromechanical properties of (d) triangle, (e) grid, and (f) honeycomb infilled samples.

Table 4. Tensile properties of the 3D-printed samples.

Sample	Tensile strength [MPa]	Elongation at break [%]	Young's modulus at 100% elongation [MPa]
C-TR10	12.87 ± 0.83	549.75 ± 31.69	11.16 ± 3.69
C-TR15	11.51 ± 2.35	514.60 ± 51.40	21.76 ± 4.20
C-TR20	12.54 ± 1.09	430.97 ± 6.98	24.63 ± 2.73
C-GD10	15.59 ± 1.19	729.40 ± 67.60	20.20 ± 4.91
C-GD15	14.47 ± 0.86	639.10 ± 36.28	26.56 ± 1.29
C-GD20	15.30 ± 1.49	657.42 ± 39.66	24.21 ± 2.43
C-HN10	15.56 ± 1.01	647.87 ± 29.18	17.06 ± 3.41
C-HN15	11.25 ± 1.10	743.52 ± 45.64	20.05 ± 2.72
C-HN20	13.77 ± 0.34	646.21 ± 77.59	17.21 ± 3.45

the material content and load-bearing area of FDM structures, the triangle pattern in this study exhibited increased node intersections and reduced strain redistribution capability at higher infill densities [14,15]. As the filament spacing decreased, the triangular nodes became more constrained, resulting in earlier stress localization and structural instability during tensile loading. These stress concentration regions likely promoted premature crack initiation and localized failure before the additional material content could effectively improve tensile strength. Similar behavior has been reported in FDM lattice and cellular structures, where mechanical performance is governed not only by material quantity but also stress also by printed line orientation, and node geometry within the printed structure [26–28]. The Young's modulus of the triangle structures increased from 11.16 MPa for C-TR10 to 24.63 MPa for C-TR20, indicating that higher infill density increased structural stiffness despite the reduction in tensile strength. The increased stiffness may restrict structural deformation during stretching, which can limit conductive pathway modulation and contribute to the lower strain sensitivity observed at higher infill densities.

The grid pattern (Figure 3(b)) exhibited the highest tensile strength among investigated structures. The maximum stresses were approximately 15.59 MPa (C-GD10), 14.47 MPa (C-GD15), and 15.30 MPa (C-GD20). In particular, C-GD10 showed the highest stress value in the study with elongation approaching ~700%, indicating that the orthogonal printed arrangement provided efficient load transfer along the tensile direction. The GD structures also exhibited relatively high Young's modulus values ranging from 20.20 MPa to 26.56 MPa, reflecting the rigid orthogonal printed line arrangement and higher structural stiffness. This efficient load transfer contributed to high tensile strength. However, the relatively stiffer structure reduced the degree of deformation-induced conductive pathway variation compared with the more compliant honeycomb structure.

For the honeycomb structure (Figure 3(c)), the maximum tensile stresses were approximately 15.56 MPa (C-HN10), 11.25 MPa (C-HN15), and 13.77 MPa (C-HN20), with elongations ranging from 650% and 750%. The C-HN20 sample exhibited the highest elongation (~750%) among all samples, but the stress dropped more rapidly after reaching the peak stress due to collapse or buckling of the honeycomb cell walls. The honeycomb lattice consists of hexagonal cells that primarily deform through bending and rotation of the cell walls rather than direct stretching, which allows the structure to accommodate large deformation with lower resistance to applied load. This deformation mechanism results in higher structural compliance and energy absorption capability compared with the C-TR and C-GD patterns, which rely more on direct filament stretching. As a result, the honeycomb structure can sustain larger elongation but typically exhibits lower ultimate stress once the cell walls begin to buckle or collapse. Similar deformation behavior of honeycomb lattices has been widely reported in cellular materials and 3D-printed structures, where structures-dominated structure exhibit higher ductility but lower strength compared with stretching-dominated structures [27,29]. The honeycomb structures exhibited comparatively lower Young's modulus values (17.06 MPa to 20.05 MPa), indicating greater structural flexibility and compliance. The lower stiffness allowed larger tensile deformation of the CNT-coated TPU structure, resulting in greater conductive pathway arrangement during stretching and contributing to the superior strain sensing performance observed for the C-HN10 sample.

3.3 Electromechanical performance

The electromechanical response curves can be divided into three sensing regions (S_1, S_2, and S_3) according to the change in slope of the ($\Delta I/I_0$) response with increasing strain as shown in Figure 3(d-f). The initial region (S_1) corresponding to the low-strain range of approximately 0% to 20% strain, exhibits the highest sensitivity due to the initial separation of neighboring CNT conductive pathways. The intermediate region (S_2), observed at approximately 20% to 50% strain, represents moderate deformation where partial rearrangement and gradual separation of conductive network occurs, resulting in a reduced response rate compared with S_1. The region (S_3), corresponding to the higher strain range of approximately 50% to 100% strain, shows lower sensitivity because the conductive network becomes more stable and changes in conductive pathway density occur more gradually. These multi-stage sensing behaviors are beneficial for detecting different magnitudes of body movement, ranging from small deformation to large joint motion during wearable sensing applications [30,31].

For the triangle pattern (Figure 3(d)), the initial sensitivity (S_1) ranged from 1.839 to 2.519, with C-TR10 showing the highest values (S_1 = 2.519). As strain increases, the sensitivity decreases to S_2 ranging from 0.781 to 0.986 and further stabilized at S_3 ranging from 0.244 to 0.305 at higher strain levels. The reduction in slope suggests that the conductivity network gradually stabilizes as the TPU structure elongates and CNT pathways align along the stretching direction. For the grid structure (Figure 3(e)), significantly higher sensitivity was observed in the low-strain region. The C-GD10 sample exhibited S_1 = 8.728, while C-GD15 and C-GD20 showed values of S_1 = 5.235, and 3.292, respectively. In the intermediate strain region, the sensitivities were S_2 = 0.224 to 0.328. The higher initial response of the grid structure can be attributed to the orthogonal printed arrangement, which allows grater separation of conductive CNT pathways during early deformation.

The honeycomb structures (Figure 3(f)) produced the highest sensitivity among all structures. The C-HN10 sample exhibited the highest initial slope with S_1 = 9.283, followed by C-HN15 (S_1 = 3.139) and C-HN20 (S_1 = 2.072). In the intermediate strain region, sensitivities decreased to S_2 = 0.554 to 1.783, and further stabilized at S_3 = 0.178 to 0.249 at higher strain levels. The superior sensing response of the honeycomb structure can be attributed to its highly deformable cellular structure and bending-dominated deformation mechanism. Unlike the triangle and grid structures, which rely primarily on stretching of the printed line, the honeycomb lattice deforms through bending, rotation and expansion of the hexagonal cell walls under tensile loading. This deformation mode allows greater structural flexibility and larger strain accommodation, resulting in more pronounced separation and rearrangement of the CNT conductive pathways during stretching. Consequently, larger variations in conductive network connectivity are generated, leading to greater changes in normalized current and higher gauge factor values. Furthermore, the honeycomb structures exhibited lower Young's modulus and greater elongation compared with the other infill patterns, which is advantageous for strain sensing applications. Similar deformation behavior has been reported in honeycomb and cellular lattice structures, where bending-dominated architectures provide enhanced structural compliance and greater deformation capability compared with stretching-dominated geometries [26–28].

Overall, lower infill densities produced higher sensing sensitivity, as the reduced structural stiffness allowed greater deformation of the CNT-coated TPU matrix. Among all configurations, the C-HN10 structure demonstrated the best sensing performance, combining the highest initial sensitivity (S_1 = 9.283) with stable electrical response across the full strain range. These results highlight the importance of infill architecture and density in tuning the electromechanical performance of 3D-printed strain sensors for wearable motion monitoring.

3.4 Cyclic electromechanical

To further evaluate the sensing stability under dynamic deformation, cyclic electromechanical tests were conducted on samples with 10% infill density for each pattern, (C-TR10, C-GD10, and C-HN10), as shown in Figure 4-5. The 10% infill condition was selected because the previous electromechanical analysis demonstrated that C-HN10 exhibited the highest sensitivity, indicating that lower infill density provides greater structural flexibility and larger variations in the conductive CNT network during deformation. Therefore, using 10% infill for all patterns allows a consistent comparison of cyclic sensing performance.

Figure 4(a-c) show the influence of deformation rate on the electromechanical response, where the sensors were tested at crosshead speeds ranging from 10 mm·min^{-1} to 30 mm·min^{-1}. The cyclic signals remained stable across all testes, indicating that the sensing performance is largely independent of deformation rate within this range. For the C-TR10 and C-GD10 structures, the signal amplitudes remained around 20% to 23% and 19% to 21%, respectively, while the C-HN10 sample maintained a higher response of 33% to 38%. The relatively stable signal amplitude observed across different loading speeds suggests that the conductive pathways remained mechanically and electrically stable within the investigated deformation-rate range.

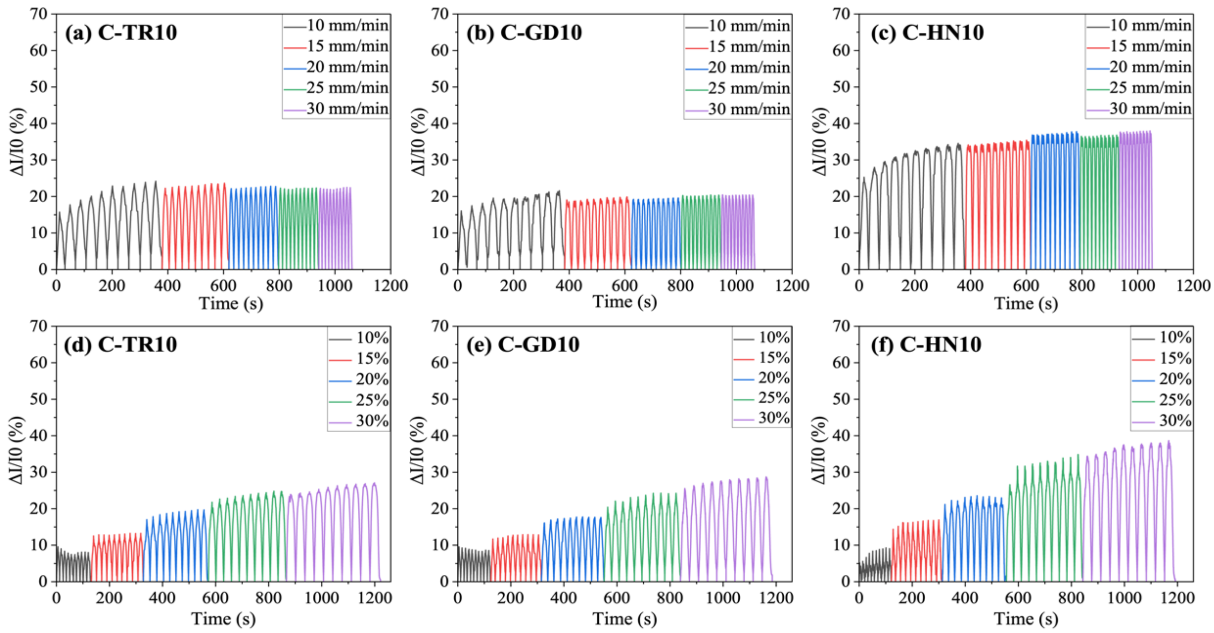

Figure 4. Cyclic electromechanical response of C-TR10, C-GD10, and C-HN10 samples under (a-c) varying deformation rates (10 mm·min^{-1} to 30 mm·min^{-1}), and (d-f) different strain levels (10% to 30%).

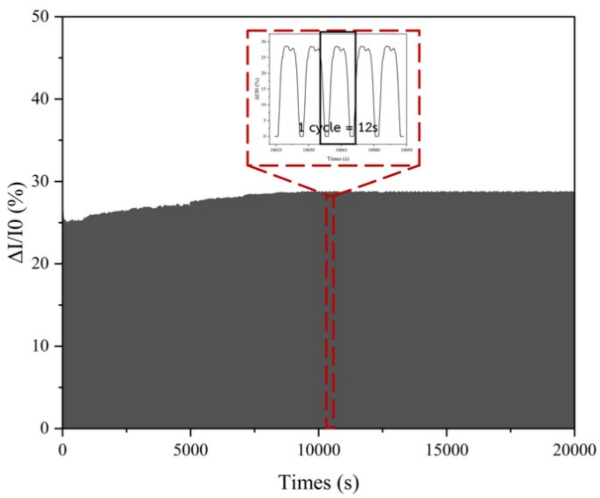

Figure 5. Long-term cyclic electromechanical stability of the C-HN10 sensor under repeated tensile loading.

Figure 4(d-f) show the cycle electrical response of the sensor under increasing strain levels from 10% to 30% at a constant crosshead speed of 10 mm·min^{-1}. For all three patterns, the normalized current change ($\Delta I/I_0$) increased systematically with increasing strain amplitude, indicating a strong correlation between electrical signal and mechanical deformation. At 10% strain, the signal amplitude was approximately 7% to 10% across the samples. When the strain increased to 15%, the electrical response rose to 12% to 16%, followed by 18% to 23% at 20% strain. At higher strain levels of 25% and 30%, the signal amplitude further increased, reaching approximately 22% to 28% for C-TR10 and C-GD10, while the C-HN10 structure exhibited the largest response of 30% to 38%. In addition to the increasing amplitude, the signals remained highly repeatable with clear and consistent loading-unloading cycles, indicating stable conductive pathways during repeated deformation.

Moreover, the cyclic electromechanical stability of the HN10 sample under repeated tensile loading is shown in Figure 5. The long-term stability test was conducted at 30% strain with a crosshead speed of

10 mm·min^{-1} for approximately 20,000 s, corresponding to ~1,425 loading-unloading cycles. The normalized current change exhibits a stable response throughout the testing period, with a slight initial increase from approximately 25% to 30%, followed by a steady plateau, indicating stabilization of the CNT conductive network. The inset shows consistent loading-unloading cycles at different time intervals, with nearly identical peak amplitudes and signal shapes. No significant signal degradation or baseline drift was observed throughout the test. This stability is likely associated with the ultrasonication-assisted coating and thermal treatment process, which promoted strong CNT attachment and partial penetration into the surface and interlayer region of the TPU substrate. Although minor conductive network rearrangement may occur during cyclic loading, no evidence of severe conductive failure was observed under the investigated testing conditions.

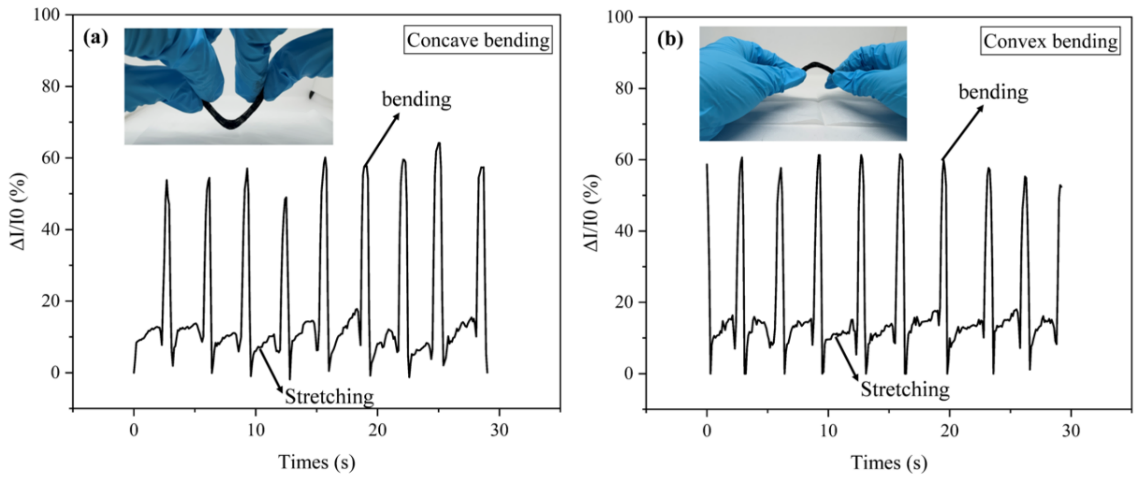

Figure 6. Electromechanical response of the C-HN10 sensor under (a) concave, and (b) convex bending.

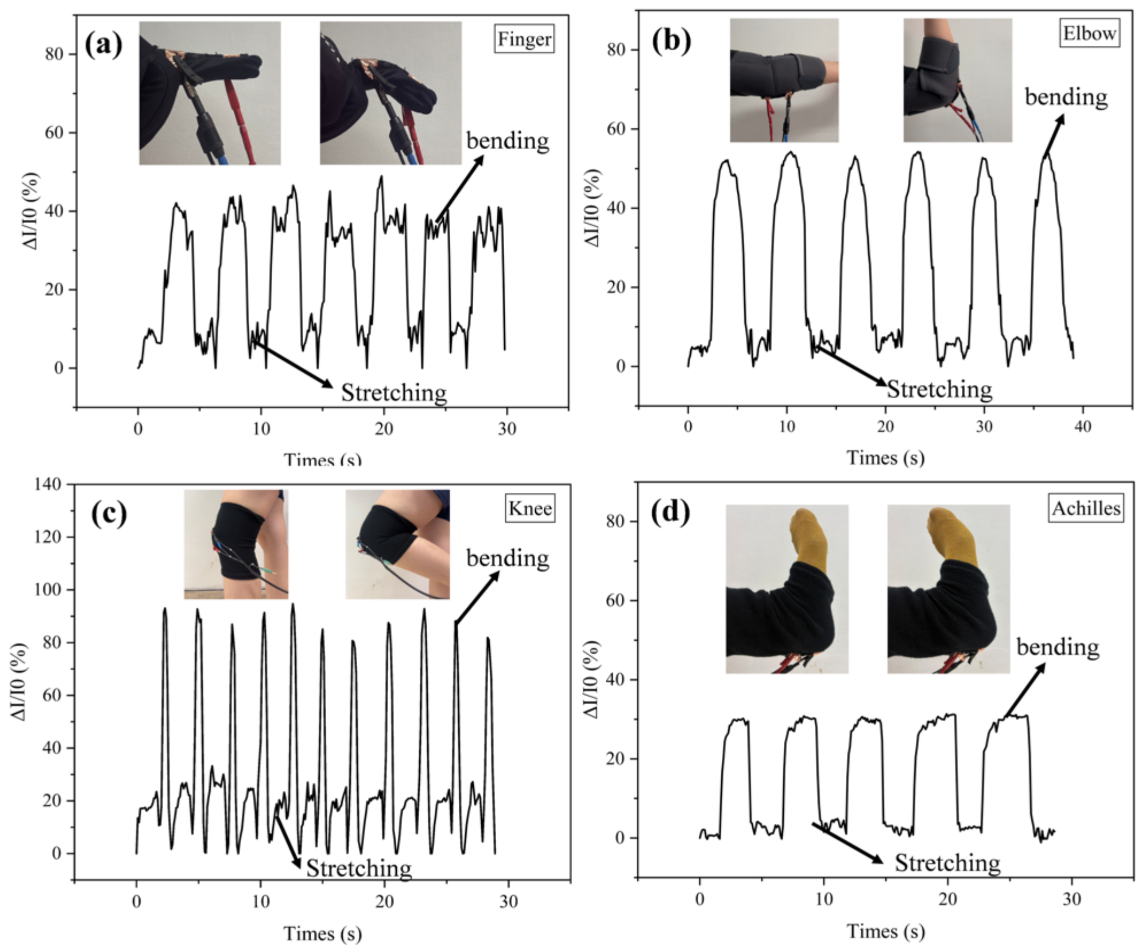

Figure 7. Electromechanical response of the C-HN10 sensor during dynamic body movements measured at different joints (a) finger, (b) elbow, (c) knee, and (d) achilles.

Table 5. Comparison of 3D-printed CNT-based wearable strain sensors reported in the literature.

Reference	Conductive material	3D Printing technique	Processing approach	Motion detection demonstration	Key findings
Christ *et al.* [21]	CNT/TPU nanocomposite	FDM	CNT-reinforced conductive filament	Tensile strain sensing	Demonstrated highly elastic 3D-printed strain sensors with excellent flexibility and repeatable electromechanical response.
Xiang *et al.* [22]	CNT/TPU nanocomposite	FDM	CNT-reinforced conductive filament with non-covalent interaction enhancement	Tensile strain sensing	Improved CNT dispersion and interfacial interaction resulted in enhanced sensitivity and sensing stability.
Luo *et al.* [23]	CNT/TPU composite	FDM	CNT-reinforced conductive filament	Finger, wrist, and knee motion monitoring	High-performance flexible strain sensor with excellent stretchability and wearable motion-monitoring capability.
Li *et al.* [25]	CNT-coated TPU	FDM + Ultrasonic cavitation	Ultrasonication-assisted CNT surface coating on auxetic TPU substrate	Finger and wrist motion monitoring	Surface CNT coating preserved TPU flexibility while providing stable electromechanical performance for wearable sensing.
Present work	CNT-coated TPU	FDM	Ultrasonication-assisted CNT surface coating on printed TPU substrate	Finger, elbow, knee, and achilles tendon motion monitoring	Tunable sensing performance through infill geometry design (triangle, grid, and honeycomb).

3.5 Electromechanical response under human body movement

To evaluate the practical sensing capability of the optimized C-HN10 strain sensor, its electromechanical response was first examined under control bending conditions as shown in Figure 6 and subsequently under body motion as shown in Figure 7.

Figure 6 shows the electrical response of the sensors under concave (Figure 6(a)) and convex bending (Figure 6(b)). In both cases, the sensor generated clear and repeatable electrical signals corresponding to each bending cycle. During concave bending, the sensor experienced tensile deformation along the outer surface, resulting in a sharp increase in the normalized current change. The peak signal amplitude reached approximately 55% to 65%, with consistent peak shapes observed throughout repeated bending cycles. Similarly, under convex bending, the sensor produced stable and repeatable signals with amplitudes of 55% to 60%. Although the overall signal magnitudes were comparable for both bending modes, slight variations in peak intensity were observed due to differences in strain distribution along the sensor during opposite bending directions. The consistent recovery of the baseline after each cycle indicates good mechanical flexibility and reversible electrical response of the CNT-coated TPU structure.

Following the controlled bending tests, the sensor was sewn into knitted bands to evaluate its response under body movement such as finger, elbow, knee and achilles bending, as shown in Figure 7. The recorded signals show clear and periodic changes in ($\Delta I/I_0$) corresponding to repeated joint bending and releasing motions. The signal amplitudes varied depending on the degree of deformation, with values ranging from 30% to 100%, reflecting the different strain levels experienced by the sensor during movement. Despite the variation in signal magnitude, all motions produced distinct and repeatable electrical responses with minimal signal drift, demonstrating stable sensing behavior under dynamic conditions. The strong signal response observed during both bending tests and body movement can be attributed to the high flexibility of the TPU matrix combined with the conductive CNT network deposited on the surface. When the structure is deformed, the distance between neighboring CNT pathways changes, leading to variations in electrical current. Upon release of the deformation, the TPU matrix elastically recovers, and the conductive network reconnects, restoring the electrical signal. Compared with previously reported 3D-printed CNT-based wearable strain sensors, the present work employs a different processing based on ultrasonication-assisted CNT surface coating on FDM printed TPU substrates. As shown in Table 5, many previous studies relied on conductive composite filaments prepared through direct CNT incorporation into the polymer matrix, the proposed approach introduces conductivity through surface coating while preserving the intrinsic flexibility of the TPU substrate. In addition, the sensing performance can be tailored through infill geometry design, providing an additional structural parameter for sensor optimization. The successful monitoring of finger, elbow, knee, and achilles tendon movements further demonstrates the versatility of the proposed sensor for wearable motion monitoring. While the proposed sensor demonstrated promising motion-monitoring capability, additional studied are still required to evaluate its long-term practical applicability. In particular, washing, durability, environmental stability under varying temperature and humidity conditions, long-term wearable performance, and benchmarking against commercial wearable strain sensors remain important areas for future investigation. Further development may also focus on improving coating durability and further optimizing sensor integration into wearable platforms.

4. Conclusions

The combination of 3D-printed TPU substrates and CNT incorporation provides an effective approach to develop flexible strain sensors with tunable mechanical and electromechanical performance. The results demonstrate that infill pattern and density strongly influence sensor behavior, where structural design governs deformation characteristics and conductive network evolution. Among the investigated configurations, the honeycomb pattern with 10% infill (C-HN10) exhibited the best performance, offering high flexibility, high elongation, and enhanced strain sensitivity due to its compliant structure and efficient modulation of conductive pathways under strain. The ultrasonication-assisted CNT treatment, followed by thermal processing, enabled uniform CNT deposition and partial embedding within the TPU surface and interlayer gaps, as confirmed by SEM and EDS analysis. This conductive network contributed to stable and repeatable electrical responses during tensile deformation. Cyclic testing further demonstrated excellent durability, with minimal signal degradation over extended loading conditions. Additionally, the sensor maintained consistent and reliable responses under bending deformation and when integrated into wearable bands for motion detection.

Acknowledgements

The authors would like to thank all participants involved in this study for their time and cooperation. The authors also gratefully acknowledge the Department of Materials Science, Faculty of Science, Chulalongkorn University for providing the facilities and technical support necessary to carry out this research.

References

[1] A. Yadav, N. Yadav, Y. Wu, S. RamaKrishna, and Z. Hongyu, "Wearable strain sensors: state-of-the-art and future applications," *Materials Advances*, vol. 4, no. 6, pp. 1444–1459, 2023.

[2] T. Q. Trung, and N.-E. Lee, "Flexible and stretchable physical sensor integrated platforms for wearable human-activity monitoring and personal healthcare," *Advanced Materials*, vol. 28, no. 22, pp. 4338–4372, 2016.

[3] M. Amjadi, K.-U. Kyung, I. Park, and M. Sitti, "Stretchable, skin-mountable, and wearable strain sensors and their potential applications: A review," *Advanced Functional Materials*, vol. 26, no. 11, pp. 1678–1698, 2016.

[4] Y. Li, S. Pei, J. Wang, C. Zhang, B. Shi, and Z. Luo, "Wearable sensors fabricated by 3D-printed composite hydrogel with 2D fillers," *Small Methods*, vol. 10, no. 4, p. e02195, 2026.

[5] J. Chen, H. Li, Q. Yu, Y. Hu, X. Cui, Y. Zhu, and W. Jiang, "Strain sensing behaviors of stretchable conductive polymer composites loaded with different dimensional conductive fillers," *Composites Science and Technology*, vol. 168, pp. 388–396, 2018.

[6] W. Obitayo, and T. Liu, "A review: carbon nanotube-based piezoresistive strain sensors," *Journal of Sensors*, vol. 2012, no. 1, p. 652438, 2012.

[7] Y. Yi, B. Wang, X. Liu, and C. Li, "Flexible piezoresistive strain sensor based on CNTs–polymer composites: A brief review," *Carbon Letters*, vol. 32, no. 3, pp. 713–726, 2022.

[8] S. Cravanzola, G. Haznedar, D. Scarano, A. Zecchina, and F. Cesano, "Carbon-based piezoresistive polymer composites: Structure and electrical properties," *Carbon*, vol. 62, pp. 270–277, 2013.

[9] M. M. Hossain, P. Kungsadalpipob, N. He, W. Gao, and P. Bradford, "Multilayer core-shell fiber device for improved strain sensing and supercapacitor applications," *Small*, vol. 20, no. 38, p. 2401031, 2024.

[10] C. Harito, D. V Bavykin, B. Yuliarto, H. K. Dipojono, and F. C. Walsh, "Polymer nanocomposites having a high filler content: synthesis, structures, properties, and applications," *Nanoscale*, vol. 11, no. 11, pp. 4653–4682, 2019.

[11] X. Zhao, J. Li, M. Jiang, W. Zhai, K. Dai, C. Liu, and C. Shen, "Flexible strain sensor based on CNTs/CB/TPU conductive fibrous film with wide sensing range and high sensitivity for human biological signal acquisition," *Polymer*, vol. 302, p. 127049, 2024.

[12] I. Ayedi, and O. Kanoun, "High-performance filament strain sensor based on CNT-TPU-TPS with a double percolation network," in *2025 IEEE 22nd International Multi-Conference on Systems, Signals & Devices (SSD)*, 2025, pp. 557–561.

[13] H. Nie, Z. Chen, H. Tang, Y. Ren, and W. Liu, "Strain sensor based on polyurethane/carbon nanotube elastic conductive spiral yarn with high strain range and sensitivity," *Polymer Composites*, vol. 45, no. 6, pp. 5522–5531, 2024.

[14] L. Rodríguez-Parada, S. de la Rosa, and P. F. Mayuet, "Influence of 3D-printed TPU properties for the design of elastic products," *Polymers*, vol. 13, no. 15, p. 2519, 2021.

[15] L. Rodríguez, G. Naya, and R. Bienvenido, "Study for the selection of 3D printing parameters for the design of TPU products," *IOP Conference Series: Materials Science and Engineering*, vol. 1193, no. 1, p. 012035, 2021.

[16] K. Kim, J. Park, J. Suh, M. Kim, Y. Jeong, and I. Park, "3D printing of multiaxial force sensors using carbon nanotube (CNT)/thermoplastic polyurethane (TPU) filaments," *Sensors and Actuators A: Physical*, vol. 263, pp. 493–500, 2017.

[17] F. Stan, N. Stanciu, A.-M. Constantinescu, and C. Fetecau, "3D printing of flexible and stretchable parts using multiwall carbon nanotubes/polyester-based thermoplastic polyurethane," in *ASME 2020 15th International Manufacturing Science and Engineering Conference*, 2020.

[18] Y. Zhou, S. Liu, F. Zhang, S. Deng, Y. Wang, J. Wang, H. Wu, Q. Wang, and L. Xing, "Fabrication of CNT/Ni/PLA/TPU composites via FDM and their electromagnetic-wave absorption performance," *Journal of Alloys and Compounds,* vol. 1041, p. 183789, 2025.

[19] G. Sui, D. Liu, Y. Liu, W. Ji, Q. Zhang, and Q. Fu, "The dispersion of CNT in TPU matrix with different preparation

methods: solution mixing vs melt mixing," *Polymer,* vol. 82, p. 121838, 2019.

[20] J. Sharifi, G. Rizvi, and H. (Ramona) Fayazfar, "Sustainable 3D printing of enhanced carbon nanotube-based polymeric nanocomposites: green solvent-based casting for eco-friendly electrochemical sensing applications," *The International Journal of Advanced Manufacturing Technology*, vol. 131, no. 9, pp. 4825–4837, 2024.

[21] J. F. Christ, N. Aliheidari, A. Ameli, and P. Pötschke, "3D printed highly elastic strain sensors of multiwalled carbon nanotube/thermoplastic polyurethane nanocomposites," *Materials and Design*, vol. 131, pp. 394–401, 2017.

[22] D. Xiang, X. Zhang, Y. Li, E. Harkin-Janes, Y. Zheng, L. Wang, C. Zhao, and P. Wang, "Enhanced performance of 3D printed highly elastic strain sensors of carbon nanotube/thermoplastic polyurethane nanocomposites via non-covalent interactions," *Composites Part B: Engineering.*, vol. 176, p. 107250, 2019.

[23] X. Luo, H. Cheng, K. Chen, L. Gu, S. Liu, and X. Wu, "Multiwalled carbon nanotube-enhanced polyurethane composite materials and the application in high-performance 3D printed flexible strain sensors," *Composites Science and Technology*, vol. 257, p. 110818, 2024.

[24] S. Wu, P. Potiyaraj, C. Aumnate, and P. Kungsadalpipob, "Tailored carbon nanotubes (CNTs)/thermoplastic polyurethane (TPU) composite pressure sensors via optimized 3D printing for smart wearable electronics," *Journal of Materials Research and Technology*, vol. 42, pp. 9640–9653, 2026.

[25] B. Li, W. Liang, L. Zhang, F. Ren, and F. Xuan, "TPU/CNTs flexible strain sensor with auxetic structure via a novel hybrid manufacturing process of fused deposition modeling 3D printing and ultrasonic cavitation-enabled treatment," *Sensors and Actuators A: Physical*, vol. 340, p. 113526, 2022.

[26] B. Rankouhi, S. Javadpour, F. Delfanian, and T. Letcher, "Failure analysis and mechanical characterization of 3D printed ABS with respect to layer thickness and orientation," *Journal of Failure Analysis and Prevention*, vol. 16, no. 3, pp. 467–481, 2016.

[27] R. Liu, W. Chen, and J. Zhao, "A review on factors affecting the mechanical properties of additively-manufactured lattice structures," *Journal of Materials Engineering and Performance*, vol. 33, no. 10, pp. 4685–4711, 2024.

[28] Y. Li, D. Jiang, R. Zhao, X. Wang, L. Wang, and L.-C. Zhang, "High mechanical performance of lattice structures fabricated by additive manufacturing," *Metals*, vol. 14, no. 10, p. 1165, 2024.

[29] X. Shu, Y. Mao, M. Lei, D. Da, S. Hou, and P. Zhang, "Toughness enhancement of honeycomb lattice structures through heterogeneous design," *Materials and design*, vol. 217, p. 110604, 2022.

[30] N. I. Sonil, Z. Ullah, J. Chen, and G. P. Wang, "Wearable strain sensors for human motion detection and health monitoring based on hybrid graphite-textile flexible electrodes," *Journal of Materials Research and Technology*, vol. 26, pp. 764–774, 2023.

[31] Y. Bai, Y. Zhou, X. Wu, M. Yin, L. Yin, S. Qu, F. Zhang, K. Li, and Y. A. Huang, "Flexible strain sensors with ultra-high sensitivity and wide range enabled by crack-modulated electrical pathways," *Nanomicro Lett.*, vol. 17, no. 1, p. 64, 2024.